PHYSICAL REVIEW B **98**, 174105 (2018)

Giant direct and inverse electrocaloric effects in multiferroic thin films

Claudio Cazorla[1] and Jorge Íñiguez[2,3]
[1]*School of Materials Science and Engineering, UNSW Australia, Sydney NSW 2052, Australia*
[2]*Materials Research and Technology Department, Luxembourg Institute of Science and Technology (LIST), L-4362 Esch/Alzette, Luxembourg*
[3]*Physics and Materials Science Research Unit, University of Luxembourg, L-4422 Belvaux, Luxembourg*

(Received 15 July 2018; revised manuscript received 24 September 2018; published 9 November 2018)

Refrigeration systems based on the compression of greenhouse gases are environmentally threatening and cannot be scaled down to on-chip dimensions. In the vicinity of a phase transition, caloric materials present large thermal responses to external fields, which makes them promising for developing alternative solid-state cooling devices. Electrocaloric effects are particularly well suited for portable refrigeration applications; however, most electrocaloric materials operate best at nonambient temperatures or require the application of large electric fields. Here, we predict that modest electric fields can yield giant room-temperature electrocaloric effects in multiferroic $BiCoO_3$ (BCO) thin films. Depending on the orientation of the applied field, the resulting electrocaloric effect is either direct (heating) or inverse (cooling), which may enable the design of enhanced refrigeration cycles. We show that spin-phonon couplings and phase competition are the underlying causes of the disclosed caloric phenomena. The dual electrocaloric response of BCO thin films can be effectively tuned by means of epitaxial strain, and we anticipate that other control strategies such as chemical substitution are also possible.

DOI: 10.1103/PhysRevB.98.174105

I. INTRODUCTION

Caloric materials react thermally to external fields as a result of induced transformations involving sizable entropy changes. Their compactness and fast response to external stimuli raise high hopes to surpass the performance, environmental compliance, and portability of current refrigeration technologies based on compression cycles of greenhouse gases. A major breakthrough occurred in the late 1990's with the discovery of giant magnetocaloric effects in $Gd_5(Si_2Ge_2)$ [1]. Yet, most magnetocaloric materials are based on scarce rare-earth elements and require the generation of high magnetic fields. Meanwhile, mechanocaloric effects are attracting much attention due to their large latent heat and adiabatic temperature changes [2–6]. The practical implementation of mechanocaloric effects, however, becomes difficult when scaling down towards on-chip dimensions.

In the context of microelectronic cooling, electrocaloric (EC) materials emerge as particularly promising owing to their high-energy density, natural integration in circuitry [7–15], and the possibility of implementing charge-recovery strategies to increase efficiency [16]. Unfortunately, the largest EC effects observed to date occur at high temperatures [17] or require large electric fields [18], which may lead to the appearance of impeding leakage current and dielectric loss problems [16,19]. Here, we demonstrate giant room-temperature EC effects ($|\Delta T| \sim 10$ K) in epitaxially grown $BiCoO_3$ (BCO) thin films induced by modest electric fields ($\sim$100 kV cm^{-1}). We use first-principles methods [20,21] to resolve the phase diagram of BCO thin films and show that it is possible to obtain field-driven transitions from a nonpolar antiferromagnetic (AFM) phase to either a high-entropy polar paramagnetic (PM) phase (inverse effect, $\Delta T < 0$) or a low-entropy polar AFM phase (direct effect, $\Delta T > 0$), depending on the orientation of the applied electric field. We show that the causes of the disclosed EC phenomena are strong phase competition and spin-phonon couplings.

II. METHODS

A. First-principles calculations

In our first-principles calculations, we use the generalized gradient approximation of Perdew-Burke-Ernzerhof (GGA-PBE) to density functional theory (DFT) [22,23] because this functional provides an accurate description of the relative stability of bulk BCO polymorphs at zero temperature [20]. A Hubbard-U scheme with $U = 6$ eV is employed for a better treatment of Co's 3d electrons [20]. We use the projector augmented-wave method to represent the ionic cores [24], considering the following electrons as valence states: Co's 3p, 3d, and 4s; Bi's 5d, 6s, and 6p; and O's 2s and 2p. Wave functions are represented in a plane-wave basis truncated at 650 eV, and for integrations within the first Brillouin zone (BZ) we employ a dense Γ-centered q-point grid of $12 \times 12 \times 12$ for a $2 \times \sqrt{2} \times \sqrt{2}$ supercell containing 20 atoms (i.e., 4 formula units) [25,26]. By using these parameters we obtain zero-temperature energies converged to within 0.5 meV per formula unit. Our strained-bulk geometry relaxations are performed with a conjugate-gradient algorithm that allows for volume variations while imposing the structural constraints defining (100)-oriented perovskite thin films [25,26]. The relaxations are halted when the forces in the atoms all fall below 0.01 eV Å^{-1}. The calculation of phonon frequencies is performed with the small displacement method [27,28]. We find the following settings to provide quasiharmonic free energies converged to within 5 meV per formula unit: 160-atom supercells, atomic displacements of 0.02 Å, and q-point grids of $16 \times 16 \times 16$ for BZ integrations.

B. Estimation of free energies and EC effects

We calculate the Helmholtz free energy of competitive polymorphs in (001)-oriented BCO thin films as a function of temperature (T) and in-plane lattice parameter ($a_{\rm in}$) with first-principles methods (see Refs. [20,21] and the Appendix). Our approach takes into account the couplings between magnetic spin disorder and lattice phonons, which strongly depend on temperature and epitaxial strain. We start by expressing the internal energy of the thin film as

$$\tilde{E}_{\rm harm}(T, a_{\rm in}) = \tilde{E}_0(T, a_{\rm in}) + \frac{1}{2}\sum_{mn} \tilde{\Xi}_{mn}(T, a_{\rm in}) u_m u_n, \tag{1}$$

where $\tilde{E}_0$ represents an effective static energy, $\tilde{\Xi}_{mn}$ an effective force-constant matrix (see the Appendix), u's atomic displacements, and the dependences of the various terms on T and $a_{\rm in}$ are explicitly noted. The Helmoltz free energy associated with the lattice vibrations, $\tilde{F}_{\rm vib}$, is calculated by finding the phonon eigenfrequencies of the dynamical matrix obtained from $\tilde{\Xi}_{mn}$, namely, $\tilde{\omega}_{\mathbf{q}s}$, and subsequently using the formula [26,29]

$$\tilde{F}_{\rm vib}(T, a_{\rm in}) = \frac{1}{N_q} k_B T \sum_{\mathbf{q}s} \ln\left[2 \sinh\left(\frac{\hbar \tilde{\omega}_{\mathbf{q}s}}{2k_{\rm B}T}\right)\right], \tag{2}$$

where N_q is the total number of wave vectors used for integration in the BZ, and the summation runs over all wave vectors $\mathbf{q}$ and phonon branches s. The magnetic free energy stemming exclusively from spin fluctuations is estimated through the analytical mean-field solution to the spin-$\frac{1}{2}$ Ising model at zero magnetic field [30], which reads

$$\tilde{F}_{\rm mag}(T, a_{\rm in}) = -k_B T \left[\ln 2 + \ln\cosh\frac{qJm}{2k_B T}\right] + \frac{q}{2} J m^2, \tag{3}$$

where q represents the number of nearest-neighboring spins, $J(a_{\rm in})$ the exchange constant between nearest-neighboring spins, and $m(T, a_{\rm in})$ the magnetization of the system. In practice, we estimate the value of the magnetic exchange constants from zero-temperature DFT calculations (see the Appendix) and the magnetization of the system through DFT-based spin-model Monte Carlo simulations (see the next section). The total Helmholtz free energy of the system then is estimated as

$$\tilde{F}_{\rm harm}(T, a_{\rm in}) = \tilde{E}_0(T, a_{\rm in}) + \tilde{F}_{\rm vib}(T, a_{\rm in}) + \tilde{F}_{\rm mag}(T, a_{\rm in}). \tag{4}$$

Temperature-induced phase transitions are determined via the condition $\tilde{F}^A_{\rm harm}(T_c, a_{\rm in}) = \tilde{F}^B_{\rm harm}(T_c, a_{\rm in})$, where A and B represent two different phases.

The isothermal entropy change that a polar material undergoes under the action of a varying external electric field is [31]

$$\Delta S(T, a_{\rm in}) = \int_0^{\mathcal{E}} \left(\frac{dP}{dT}\right)_{\mathcal{E}'} d\mathcal{E}', \tag{5}$$

where P represents the polarization of the system and $\mathcal{E}$ the applied electric field. Likewise, the corresponding adiabatic temperature change can be estimated as [32]

$$\Delta T(T, a_{\rm in}) = -\frac{T}{C_0} \Delta S(T, a_{\rm in}), \tag{6}$$

where $C_0(T, a_{\rm in})$ is the heat capacity of the system at zero electric field. ΔS and ΔT become large when the system undergoes a $\mathcal{E}$-induced phase transition; if such a phase transition is of first-order type, as it occurs in BCO [33,34], the isothermal entropy change can be estimated with the Clausius-Clapeyron method as [31]

$$\Delta S(T, a_{\rm in}) = -\Delta P \frac{d\mathcal{E}_c}{dT}, \tag{7}$$

where $\Delta P(T, a_{\rm in})$ is the change in polarization along the electric field direction, and $\mathcal{E}_c(T, a_{\rm in})$ the critical electric field inducing the phase transformation.

In the presence of an electric field the thermodynamic potential that appropriately describes the stability of a particular phase is the Gibbs free energy, defined as $\tilde{G}_{\rm harm} = \tilde{F}_{\rm harm} - \boldsymbol{\mathcal{E}} \cdot \boldsymbol{P}$, where $\tilde{F}_{\rm harm}$ corresponds to the Helmholtz free energy in Eq. (4). In this case, the thermodynamic condition that determines a $\mathcal{E}$-induced phase transition is $\tilde{G}^A_{\rm harm}(T, a_{\rm in}, \mathcal{E}_c) = \tilde{G}^B_{\rm harm}(T, a_{\rm in}, \mathcal{E}_c)$. The value of the corresponding critical electric field then is estimated as

$$\mathcal{E}_c(T, a_{\rm in}) = \frac{\Delta \tilde{F}_{\rm harm}(T, a_{\rm in})}{\Delta P(T, a_{\rm in})}, \tag{8}$$

where $\Delta \tilde{F}_{\rm harm}$ is the Helmholtz free-energy difference between the two phases, and ΔP the resulting change in the electric polarization along the electric field direction. By using the formulas (6)–(8) and knowing $\Delta \tilde{F}_{\rm harm}$, one can calculate ΔS and ΔT as a function of temperature and in-plane lattice parameter.

C. Spin-model Monte Carlo simulations

To simulate the effects of thermal excitations on the magnetic order of energetically competitive polymorphs in (100)-oriented BCO thin films, we construct several spin Heisenberg models of the form $\hat{H} = \frac{1}{2}\sum_{ij} J^{(0)}_{ij} S_i S_j$ based on density functional calculations (see the Appendix). We use those models to perform Monte Carlo (MC) simulations in a periodically repeated simulation box of $20 \times 20 \times 20$ spins; thermal averages are computed from runs of 50 000 MC sweeps after equilibration. These simulations allow us to monitor the T dependence of the magnetic order via the computation of the AFM-C and AFM-G order parameters [see Fig. 1(d)], defined as $S^{\rm C} \equiv \frac{1}{N}\sum_i (-1)^{n_{ix}+n_{iy}} S_{iz}$ and $S^{\rm G} \equiv \frac{1}{N}\sum_i (-1)^{n_{ix}+n_{iy}+n_{iz}} S_{iz}$. Here, n_{ix}, n_{iy}, and n_{iz} are the three integers locating the ith lattice cell, and N is the total number of spins in the simulation cell. For the calculation of $S^{\rm C}$ and $S^{\rm G}$ we consider only the z component of the spins since a small symmetry-breaking magnetic anisotropy is introduced in the system Hamiltonian to facilitate the numerical analysis.

III. RESULTS AND DISCUSSION

A. Phase transitions in BCO thin films

Figure 1 shows the relevant polymorphs of bulk BCO [20]. At ambient conditions, bulk BCO presents the ferroelectric

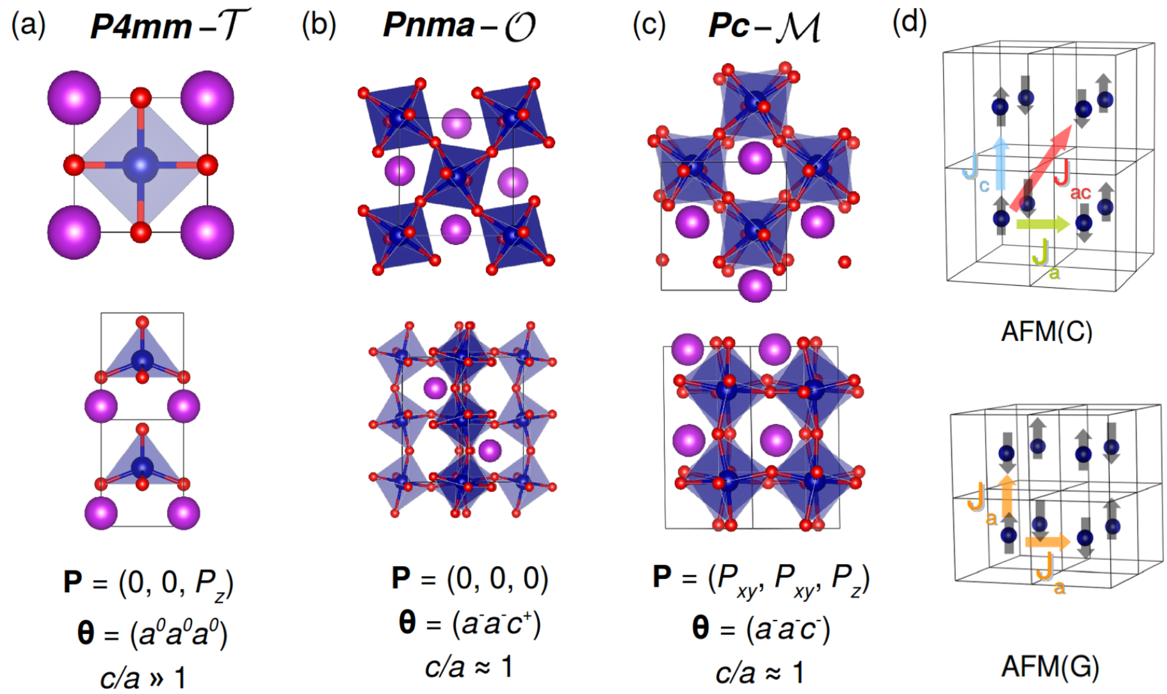

FIG. 1. Structural, ferroelectric, and magnetic properties of energetically competitive bulk BCO polymorphs. (a) Tetragonal $P4mm$ ($\mathcal{T}$), (b) orthorhombic $Pnma$ ($\mathcal{O}$), and (c) monoclinic Pc ($\mathcal{M}$). (d) Sketch of the spin configurations and exchange constants considered for the $\mathcal{T}$-AFM(C) and $\mathcal{O}$-AFM(G) Heisenberg spin models. Electrical polarizations **P** are referred to the pseudocubic Cartesian axis, and oxygen-octahedra rotation patterns $\boldsymbol{\theta}$ are expressed in Glazer's notation.

(FE) tetragonal $\mathcal{T}$ phase shown in Fig. 1(a). This structure has a relatively small in-plane lattice constant ($c/a \approx 1.3$), hence perovskite substrates with small in-plane cell parameters a_{in} will be required for stabilizing it in thin-film form. The competing structures are the paraelectric (PE) orthorhombic $\mathcal{O}$ phase [Fig. 1(b)] and the FE monoclinic $\mathcal{M}$ phase [Fig. 1(c)]; both phases have cells that are slightly distorted versions of the ideal cubic perovskite structure, with $c/a \approx 1$. Note that the mentioned FE phases present spontaneous polarizations along quite different crystallographic directions—i.e., pseudocubic $[001]_{\text{pc}}$ for $\mathcal{T}$ and $\sim[111]_{\text{pc}}$ for $\mathcal{M}$. As regards magnetism [Fig. 1(d)], both the $\mathcal{O}$ and $\mathcal{M}$ phases display G-type AFM order with a quite high Néel temperature $T_{\text{N}} \sim 500$ K. In contrast, the $\mathcal{T}$ phase presents C-type AFM order with a relatively low $T_{\text{N}} \sim 310$ K.

We thus expect the competition between BCO polymorphs to be strongly affected by epitaxially growing thin films on perovskite substrates, as this imposes an in-plane lattice constant a_{in} in the system. Our zero-temperature first-principles calculations confirm this conjecture, yielding the results summarized in Fig. 2. We predict a zero-temperature strain-driven $\mathcal{T} \rightarrow \mathcal{M}$ phase transformation at $a_{\text{in}} = 3.925$ Å [Fig. 2(a)] that involves rotation of the polarization [Figs. 2(c)and 2(e)] and the appearance of antiphase oxygen octahedral rotations along the three pseudocubic directions [Figs. 2(d) and 2(f)]. The $\mathcal{O}$ phase remains close in energy to the $\mathcal{M}$ polymorph over the whole a_{in} interval; however, it never becomes stable at zero temperature, in contrast to what occurs in compressed bulk BCO [20]. Meanwhile, the Néel temperature of epitaxially grown BCO thin films decreases mildly with increasing a_{in} [Fig. 2(b)].

We have performed first-principles Helmholtz free-energy calculations of the three relevant BCO polymorphs within the quasiharmonic approximation (see Sec. II and the Appendix), to determine their relative stability as a function of T and a_{in}. Our predicted $T - a_{\text{in}}$ phase diagram for epitaxially grown BCO thin films is shown in Fig. 3(a). For relatively small a_{in}'s, we find that the $\mathcal{T}$ phase dominates and extends its stability region to temperatures much higher than observed in bulk BCO (we recall that bulk BCO presents a $\mathcal{T} \rightarrow \mathcal{O}$ transition at $T \approx 900$ K [20]). The reason for this $\mathcal{T}$ stability enhancement is that the competing $\mathcal{O}$ polymorph remains highly strained at such a_{in} conditions [Fig. 2(a)], hence its free energy increases considerably as compared to the bulk case. As a_{in} is increased, the $\mathcal{T}$ phase eventually is replaced by the $\mathcal{O}$ and $\mathcal{M}$ polymorphs, yielding a very rich phase diagram that exhibits concurrent structural and spin-ordering transformations.

Figures 3(b)–3(d) show the calculated Helmholtz free-energy differences $\Delta\tilde{F}_{\text{harm}}$ between the three relevant BCO polymorphs expressed as a function of T and a_{in}. As noted previously, our calculations take into account all possible sources of entropy, namely, magnetic and vibrational, and the interplay between spin disorder and lattice vibrations (see Sec. II and the Appendix). We find that at high temperatures ($T \gtrsim 600$ K) the vibrational contributions to $\tilde{F}_{\text{harm}}$ always favor the $\mathcal{O}$ and $\mathcal{M}$ phases over the $\mathcal{T}$ phase. Nonetheless, whenever a polymorph becomes magnetically disordered, the corresponding Helmholtz free energy decreases significantly as a consequence of T-induced lattice phonon softenings (as is appreciated, for instance, in the densities of vibrational states calculated at $T < T_{\text{N}}$ and $T > T_{\text{N}}$, not

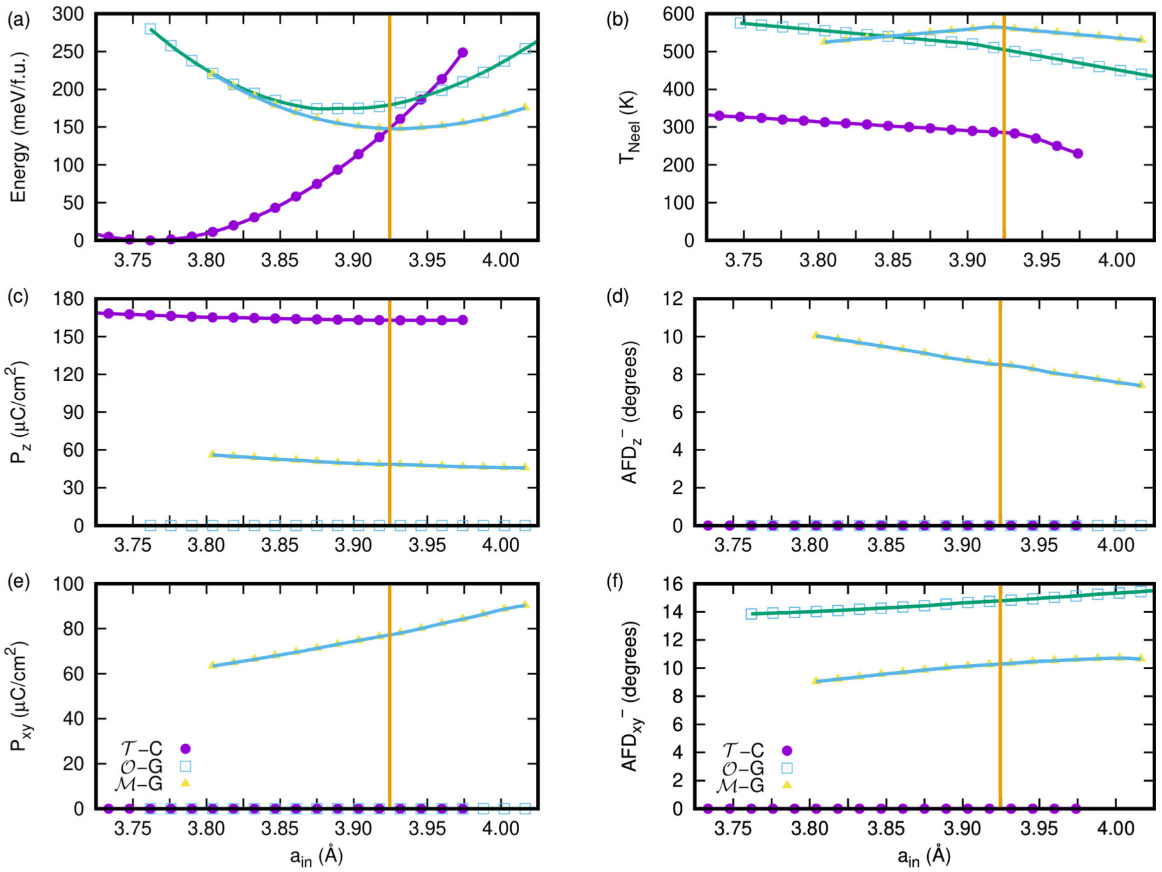

FIG. 2. Energy, magnetic, structural, and ferroelectric properties of energetically competitive polymorphs in (100)-oriented BiCoO$_3$ thin films calculated with first-principles methods. (a) Zero-temperature total energy. (b) Antiferromagnetic to paramagnetic transition temperature. (c) Electric polarization along the (100) direction. (d) Antiphase oxygen octahedral rotation angles along the (100) direction. (e) Electric polarization along the (011) direction. (f) Antiphase oxygen octahedral rotation angles along the (011) direction. The vertical lines indicate the strain-induced $\mathcal{T} \rightarrow \mathcal{M}$ phase transition occurring at very low temperatures. Electric polarizations are calculated with the Berry phase approach [35].

shown here). Accordingly, abrupt $\Delta \tilde{F}_{\rm harm}$ changes appear in Figs. 3(b)–3(d) at the corresponding AFM → PM magnetic transition temperatures. The strong spin-phonon couplings in epitaxially grown BCO thin films are responsible for the stabilization of the $\mathcal{O}$-AFM(G) phase at temperatures near ambient and 3.88 Å $\leqslant a_{\rm in} \leqslant$ 3.96 Å. Indeed, when spin-phonon couplings are disregarded (i.e., quasiharmonic free energies are calculated in the standard manner by considering "frozen" spin arrangements), the $\mathcal{O}$ phase becomes stable only after reaching the paramagnetic state at high temperatures [Figs. 3(b)–3(d) and 2(b)].

B. Electrocaloric effects in epitaxially grown BCO thin films

We now focus on the $a_{\rm in}$ region 3.89 Å $\leqslant a_{\rm in} \leqslant$ 3.93 Å, which is particularly convenient from a practical perspective since many perovskite substrates present lattice constants in this range (where all the phases remain strained by +4%–5% $\mathcal{T}$ and ±0.1%–1% $\mathcal{O}$ and $\mathcal{M}$ as compared to their corresponding equilibrium in-plane lattice parameters). Interestingly, we find a T-driven reentrant behavior that is reminiscent of bulk BCO under compression [20]: Upon heating, the BCO film transforms first from a FE [$\mathcal{T}$-AFM(C) or $\mathcal{M}$-AMF(G)] phase to a PE [$\mathcal{O}$-AFM(G)] state, then back to a FE ($\mathcal{T}$-PM) phase, and finally to a PE [$\mathcal{O}$-AFM(G)] state. Of particular interest is the PE $\mathcal{O}$-AFM(G) region appearing near room temperature $T_{\rm room}$, which is surrounded by two FE phase domains presenting markedly different features. In particular, the phase diagram in Fig. 3(a) suggests that the $\mathcal{O}$ phase may be transformed into the $\mathcal{T}$ or $\mathcal{M}$ states by applying an electric field $\mathcal{E}$ along the [001]$_{\rm pc}$ or [111]$_{\rm pc}$ directions, respectively. Such $\mathcal{E}$-driven phase transformations involve drastic structural changes as well as magnetic transitions, hence big entropy shifts are likely to occur as a consequence.

Figure 4 shows the direct EC effect associated to the field-induced $\mathcal{O} \rightarrow \mathcal{M}$ transformation [Fig. 4(a)], in which the entropy of the system decreases [$\Delta S < 0$, Fig. 4(c)]. For the smallest $a_{\rm in}$ values, a maximum adiabatic temperature change ΔT of +10 K [Fig. 4(d)] is estimated for a maximum critical electric field of 110 kV cm^{-1} [Fig. 4(b)]. The magnitude of this effect and of the accompanying critical electric field decrease with increasing $a_{\rm in}$, as the region of $\mathcal{M}$ stability is approached. Similarly, Fig. 4 shows the inverse EC effect associated to the field-induced $\mathcal{O} \rightarrow \mathcal{T}$ transformation [Fig. 4(a)], in which the entropy of the film increases [$\Delta S >$

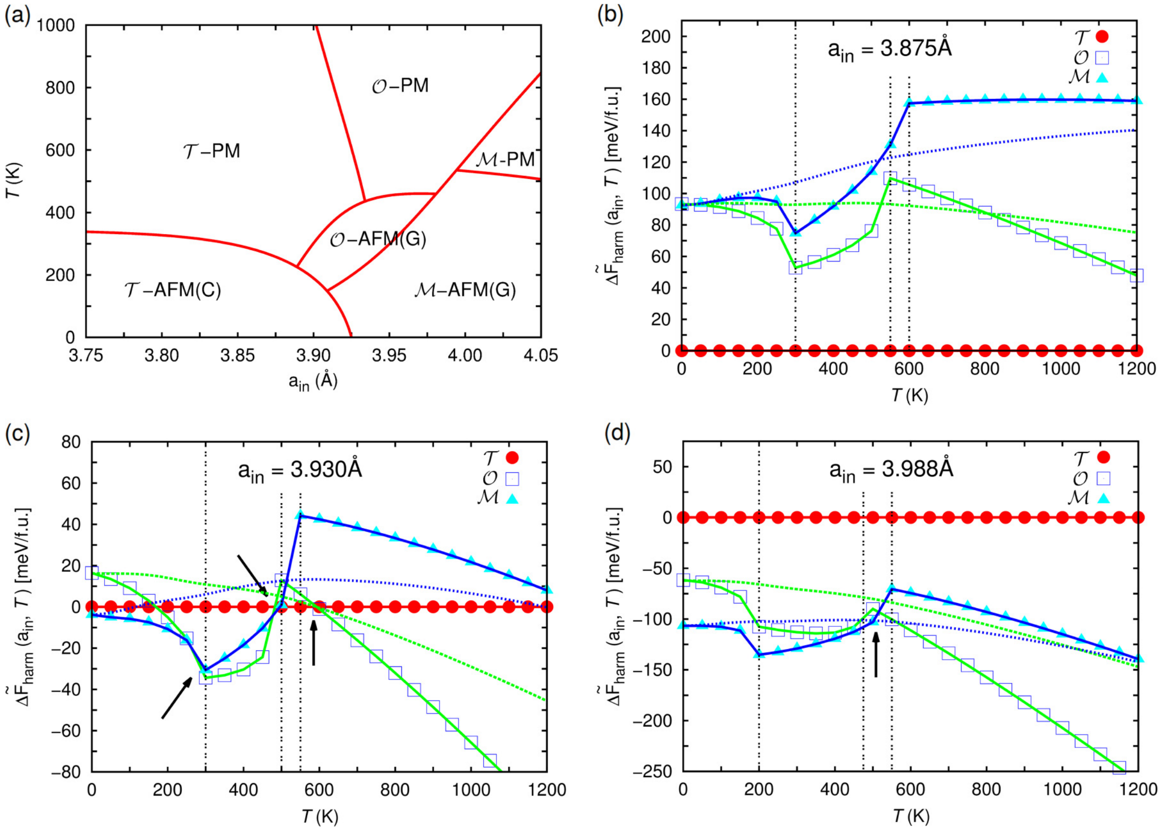

FIG. 3. $T - a_{\text{in}}$ phase diagram and free-energy differences in (100)-oriented BCO thin films. (a) Phase diagram as a function of temperature and in-plane lattice parameter. (b) Helmholtz free-energy differences among competitive polymorphs at $a_{\text{in}} = 3.875$ Å, (c) $a_{\text{in}} = 3.930$ Å, and (d) $a_{\text{in}} = 3.988$ Å. Vertical lines and black arrows indicate T-induced magnetic and structural phase transitions, respectively. Blue and green dotted lines correspond to Helmholtz free-energy differences for the $\mathcal{M}$ and $\mathcal{O}$ phases, respectively, calculated without considering spin-phonon coupling effects.

0, Fig. 4(c)]. A maximum ΔT of -50 K [Fig. 4(d)] is estimated for a maximum critical electric field of 500 kV cm^{-1} at $a_{\text{in}} = 3.93$ Å [Fig. 4(b)]. The magnitude of this effect and of the corresponding $\mathcal{E}_c$ decrease with decreasing a_{in}, as the region of $\mathcal{T}$ stability is approached. We note in passing that application of electric fields of the order of 100 kV cm^{-1} in oxide perovskite thin films appears to be nonproblematic in practice (see, for instance, Ref. [9] and experimental references therein).

The predicted giant ΔT and ΔS values, which can be achieved with relatively small driving fields, turn epitaxially grown BCO thin films into very attractive EC materials. Table I offers a comparison with other promising EC compounds. Note that BCO thin films would operate at T_{room} and display significantly larger adiabatic T spans than observed in other oxides. Meanwhile, the required electric fields are much smaller than reported for FE polymers while similar ΔT values should be attained in both cases. [The smaller heat capacity of perovskite oxides contributes favorably to this latter outcome; see Table I and Eq. (6).] Hence, BCO films somehow unite the best of the FE ceramics and FE polymer worlds. On the downside, the reported $\mathcal{E}$-driven BCO phase transitions are strongly discontinuous and thus irreversibility issues are likely to appear in practical cooling applications [31].

Let us stress that the coexistence of giant direct and inverse EC effects at room temperature offers the possibility of designing improved EC refrigeration cycles (as originally proposed by Ponomareva and Lisenkov for $\text{Ba}_{0.5}\text{Sr}_{0.5}\text{TiO}_3$ alloys [36] and subsequently discussed by Marathe *et al.* in BaTiO_3 [37]). In the present case, the coexistence of direct and inverse EC effects suggests a refrigeration cycle based on the direct transformation between the high-entropy FE $\mathcal{T}$ and low-entropy FE $\mathcal{M}$ phases as induced by $\mathcal{E}$ rotation, with a cooling performance equal to the sum of the individual $\mathcal{O} \leftrightarrow \mathcal{T}$ and $\mathcal{O} \leftrightarrow \mathcal{M}$ cycles. In addition, we foresee alternative strategies for tuning and optimizing BCO's EC behavior beyond epitaxial strain. Chemical substitution, for instance, represents an obvious option for stabilizing phases that are similar to the $\mathcal{M}$ (akin to the ground state of BiFeO_3 [25]) and $\mathcal{O}$ (most common among perovskites [38]) polymorphs discussed here, and to control the corresponding magnetic transition temperatures. One particular example is provided by $\text{BiCo}_{1-x}\text{Fe}_x\text{O}_3$ solid solutions, where a morphotropic transition between a $\mathcal{T}$-like and a $\mathcal{M}$-like phase is observed to occur at room temperature [39,40]. Likewise, bulk $\text{Bi}_{1-x}\text{La}_x\text{CoO}_3$ appears to be a good candidate to realize field-driven $\mathcal{O} \rightarrow \mathcal{T}$ transformations [20]. Hence BCO offers a variety of experimental possibilities to achieve giant EC, bringing exciting prospects to the field of solid-state cooling.

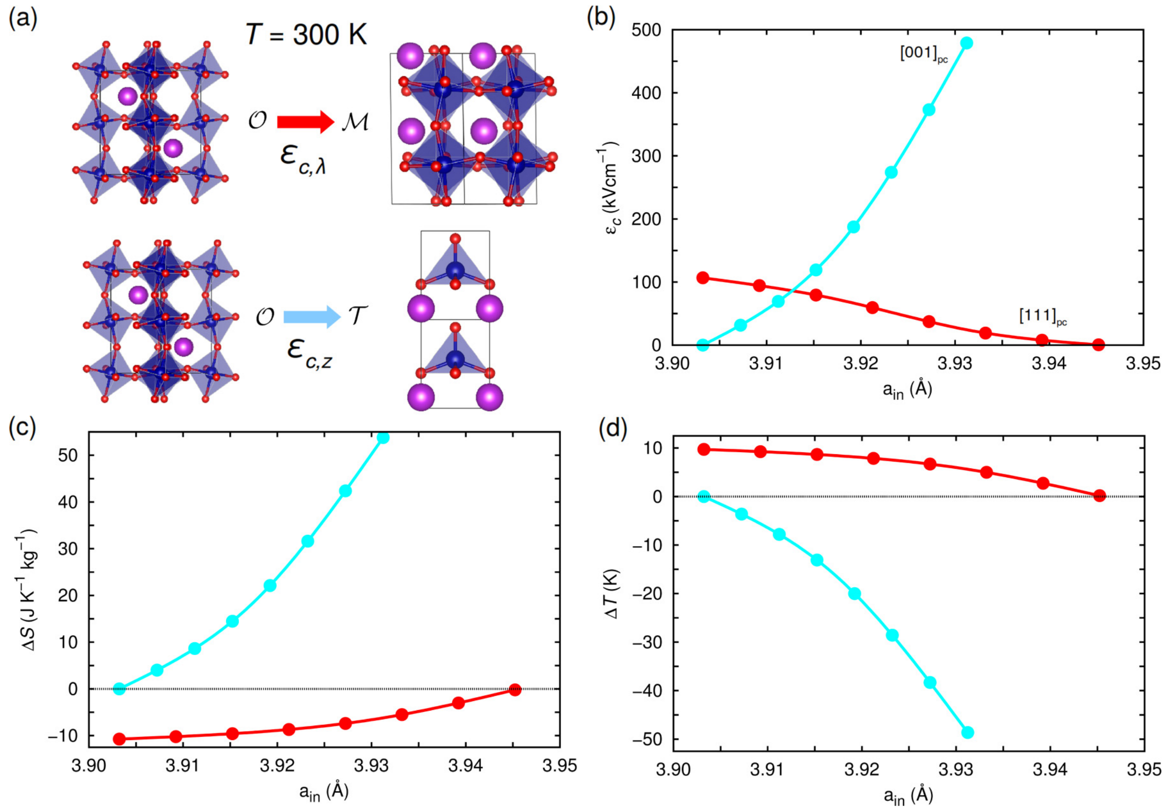

FIG. 4. Direct ($\mathcal{O} \rightarrow \mathcal{M}$, red) and inverse ($\mathcal{O} \rightarrow \mathcal{T}$, blue) electrocaloric effects in (100)-oriented BCO thin films at room temperature. (a) Sketch of the $\mathcal{E}$-induced phase transformations. (b) Critical electric field expressed as a function of in-plane lattice parameter; the two involved electric field orientations are indicated in pseudocubic Cartesian notation. (c) Room-temperature entropy and (d) adiabatic temperature shifts expressed as a function of in-plane lattice parameter.

IV. CONCLUSIONS

We have disclosed a number of multiferroic phase transitions in epitaxially grown BCO thin films that render giant and dual (that is, direct and inverse) room-temperature EC effects ($|\Delta T| \sim 10$ K) driven by moderate electric fields ($\sim$100 kV cm^{-1}). The multiferroic phase transitions and accompanying EC effects are originated by strong spin-phonon couplings and polymorph competition, which can be efficiently tuned over a wide operating-temperature interval by means of epitaxial strain. Our findings in BCO thin films should stimulate the development of cooling devices based on multiferroic EC materials, whose energy efficiency and refrigerant performance are good as compared to magnetocaloric and mechanocaloric materials. Unlike mechanocaloric materials driven by uniaxial stress or hydrostatic pressure, scalability down to transistor sizes and implementation on circuitry are possible without compromising the cooling performance. Unlike magnetocaloric compounds, the generation of large external fields at great expense is not necessary. Thus, we hope that our results in multiferroic thin films will bring different prospects to the field of solid-state cooling.

TABLE I. Electrocaloric thin film materials. T represents working temperature, $\Delta\mathcal{E}$ applied electric field (in the BCO case, we also indicate the corresponding orientation in pseudocubic Cartesian notation), C_0 heat capacity at zero field, ΔS isothermal entropy change, and ΔT adiabatic temperature change. The chemical compositions of the materials are $PbZr_{0.95}Ti_{0.05}O_3$ (PZT), poly(vinylidene fluoride-trifluoroethylene)(55/45 mol %) polymers [P(VDF-TrFE)], multilayer capacitor of doped $BaTiO_3$ (BTO-MLC), and $BiCoO_3$ (BCO).

Material	T (K)	$\Delta\mathcal{E}$ (kV cm^{-1})	C_0 (J K^{-1} kg^{-1})	ΔS (J K^{-1} kg^{-1})	ΔT (K)	Ref.
PZT	495	776	330	−8.0	+12.0	[17]
P(VDF-TrFE)	353	2000	1700	−60.0	+12.5	[18]
BTO-MLC	350	300	434	−0.7	+0.5	[8,9]
BCO	300	110 ([111]$_{pc}$)	345	−11.0	+10.0	This work
		500 ([001]$_{pc}$)		+60.0	−50.0	

ACKNOWLEDGMENTS

This research was supported under the Australian Research Council's Future Fellowship funding scheme (Project No. FT140100135) and the Luxembourg National Research Fund through the PEARL (Grant No. P12/4853155 COFERMAT) and CORE (Grant No. C15/MS/10458889 NEWALLS) programs. Computational resources and technical assistance were provided by the Australian Government and the Government of Western Australia through Magnus under the National Computational Merit Allocation Scheme and the Pawsey Supercomputing Centre.

APPENDIX: INCLUSION OF SPIN-PHONON COUPLINGS IN QUASIHARMONIC FREE-ENERGY CALCULATIONS

To calculate the Helmholtz free energy of the competitive polymorphs in (001)-oriented BCO thin films as a function of temperature (T) and in-plane lattice parameter ($a_{\rm in}$), we employ a variant of the approaches described in Refs. [20,21]. Our approach takes into consideration the couplings between magnetic spin disorder and lattice phonons, which strongly depend on the temperature and epitaxial strain conditions. Specifically, we start by expressing the internal energy of the thin film as

$$\tilde{E}_{\rm harm}(T, a_{\rm in}) = \tilde{E}_0(T, a_{\rm in}) + \frac{1}{2}\sum_{mn} \tilde{\Xi}_{mn}(T, a_{\rm in}) u_m u_n, \quad \text{(A1)}$$

where $\tilde{E}_0$ represents an effective static energy, $\tilde{\Xi}_{mn}$ an effective force-constant matrix, u's atomic displacements, and the dependences of the various terms on T and $a_{\rm in}$ are explicitly noted.

For the $\mathcal{O}$ and $\mathcal{M}$ phases ($c \approx a$), the quantities entering Eq. (A1) can be calculated as

$$\tilde{E}_0^{\mathcal{O},\mathcal{M}}(a_{\rm in}, T) = E_0(a_{\rm in}) + 3\gamma_a(a_{\rm in}, T)|S|^2 J_a^{(0)}, \quad \text{(A2)}$$

$$\tilde{\Xi}_{mn}^{\mathcal{O},\mathcal{M}}(a_{\rm in}, T) = \Phi^0_{mn}(a_{\rm in}) + 6\gamma_a(a_{\rm in}, T)|S|^2 J^{(2)}_{a,mn}, \quad \text{(A3)}$$

where $\gamma_a(a_{\rm in}, T) \equiv \langle S_i S_j\rangle/|S|^2$ represents the correlation function between neighboring spins [see Fig. 1(d)] and $\langle\cdots\rangle$ the thermal average as obtained from our Monte Carlo simulations of the corresponding spin Heisenberg Hamiltonian (see Sec. II C). The rest of the parameters in $\tilde{E}_0^{\mathcal{O},\mathcal{M}}$ and $\tilde{\Xi}_{mn}^{\mathcal{O},\mathcal{M}}$ correspond to

$$E^0 = \frac{1}{2}\left(E^{\rm FM}_{\rm eq} + E^{\rm G}_{\rm eq}\right), \quad \text{(A4)}$$

$$\Phi^0_{mn} = \frac{1}{2}\left(\Phi^{\rm FM}_{mn} + \Phi^{\rm G}_{mn}\right), \quad \text{(A5)}$$

$$J_a^{(0)} = \frac{1}{6|S|^2}\left(E^{\rm FM}_{\rm eq} - E^{\rm G}_{\rm eq}\right), \quad \text{(A6)}$$

$$J^{(2)}_{a,mn} = \frac{1}{6|S|^2}\left(\Phi^{\rm FM}_{mn} - \Phi^{\rm G}_{mn}\right). \quad \text{(A7)}$$

In the equations above, superscripts "FM" and "G" represent perfect ferromagnetic and antiferromagnetic G-type spin arrangements, respectively. The $J_a^{(0)}$ parameter describes the magnetic interactions when the atoms remain frozen at their equilibrium positions; typically, this captures the bulk of the exchange couplings. Meanwhile, the $J^{(2)}_{a,mn}$ parameter captures the dependence of the phonon spectrum on the spin configuration (i.e., spin-phonon coupling effects).

For the $\mathcal{T}$ phase ($c > a$), we express the corresponding static energy and force constant matrix as

$$\begin{aligned}\tilde{E}_0^{\mathcal{T}}(a_{\rm in}, T) = {}& E_0(a_{\rm in}) + 2\gamma_a(a_{\rm in}, T)|S|^2 J_a^{(0)} \\ & + \gamma_c(a_{\rm in}, T)|S|^2 J_c^{(0)} + 4\gamma_{ac}(a_{\rm in}, T)|S|^2 J_{ac}^{(0)},\end{aligned} \quad \text{(A8)}$$

and

$$\begin{aligned}\tilde{\Xi}^{\mathcal{T}}_{mn}(a_{\rm in}, T) = {}& \Phi^0_{mn}(a_{\rm in}) + 4\gamma_a(a_{\rm in}, T)|S|^2 J^{(2)}_{a,mn} \\ & + 2\gamma_c(a_{\rm in}, T)|S|^2 J^{(2)}_{c,mn}8 \\ & + \gamma_{ac}(a_{\rm in}, T)|S|^2 J^{(2)}_{ac,mn},\end{aligned} \quad \text{(A9)}$$

where $\gamma_\alpha(a_{\rm in}, T) \equiv \langle S_i S_j\rangle/|S|^2$, with $\alpha = a, b, ac$ representing the correlation functions between in-plane and out-of-plane neighboring spins [see Fig. 1(d)]. (We note that in this case we need to differentiate among in-plane and out-of-plane neighboring spins due to the highly anisotropic nature of the tetragonal phase.) The rest of theparameters in $\tilde{E}_0^{\mathcal{T}}$ and $\tilde{\Xi}^{\mathcal{T}}_{mn}$ can be obtained as

$$E^0 = \frac{1}{4}\left(E^{\rm FM}_{\rm eq} + E^{\rm A}_{\rm eq} + E^{\rm C}_{\rm eq} + E^{\rm G}_{\rm eq}\right), \quad \text{(A10)}$$

$$\Phi^0_{mn} = \frac{1}{4}\left(\Phi^{\rm FM}_{mn} + \Phi^{\rm A}_{mn} + \Phi^{\rm C}_{mn} + \Phi^{\rm G}_{mn}\right), \quad \text{(A11)}$$

$$J_a^{(0)} = \frac{1}{8|S|^2}\left(E^{\rm FM}_{\rm eq} + E^{\rm A}_{\rm eq} - E^{\rm C}_{\rm eq} - E^{\rm G}_{\rm eq}\right), \quad \text{(A12)}$$

$$J^{(2)}_{a,mn} = \frac{1}{8|S|^2}\left(\Phi^{\rm FM}_{mn} + \Phi^{\rm A}_{mn} - \Phi^{\rm C}_{mn} - \Phi^{\rm G}_{mn}\right), \quad \text{(A13)}$$

$$J_c^{(0)} = \frac{1}{4|S|^2}\left(E^{\rm FM}_{\rm eq} - E^{\rm A}_{\rm eq} + E^{\rm C}_{\rm eq} - E^{\rm G}_{\rm eq}\right), \quad \text{(A14)}$$

$$J^{(2)}_{c,mn} = \frac{1}{4|S|^2}\left(\Phi^{\rm FM}_{mn} - \Phi^{\rm A}_{mn} + \Phi^{\rm C}_{mn} - \Phi^{\rm G}_{mn}\right), \quad \text{(A15)}$$

$$J_{ac}^{(0)} = \frac{1}{16|S|^2}\left(E^{\rm FM}_{\rm eq} - E^{\rm A}_{\rm eq} - E^{\rm C}_{\rm eq} + E^{\rm G}_{\rm eq}\right), \quad \text{(A16)}$$

$$J^{(2)}_{ac,mn} = \frac{1}{16|S|^2}\left(\Phi^{\rm FM}_{mn} - \Phi^{\rm A}_{mn} - \Phi^{\rm C}_{mn} + \Phi^{\rm G}_{mn}\right). \quad \text{(A17)}$$

In the equations above, superscripts "FM," "G," "A," and "C" mean perfect ferromagnetic, antiferromagnetic G-type, antiferromagnetic A-type, and antiferromagnetic C-type spin arrangements, respectively. We note that the explained first-principles quasiharmonic approach could also be employed to estimate pyroelectric coefficients [41,42] in multiferroic materials.

[1] V. K. Pecharsky and K. A. Gschneidner, Jr., Giant Magnetocaloric Effect in $Gd_5(Si_2Ge_2)$, Phys. Rev. Lett. **78**, 4494 (1997).

[2] E. Bonnot, R. Romero, Ll. Mañosa, E. Vives, and A. Planes, Elastocaloric Effect Associated with the Martensitic Transition in Shape-Memory Alloys, Phys. Rev. Lett. **100**, 125901 (2008).

[3] C. Cazorla and D. Errandonea, Giant mechanocaloric effects in fluorite-structured superionic materials, Nano Lett. **16**, 3124 (2016).

[4] A. K. Sagotra, D. Errandonea, and C. Cazorla, Mechanocaloric effects in superionic thin films from atomistic simulations, Nat. Commun. **8**, 963 (2017).

[5] A. Aznar, P. Lloveras, M. Romanini, M. Barrio, J. Ll. Tamarit, C. Cazorla, D. Errandonea, N. D. Mathur, A. Planes, X. Moya, and Ll. Mañosa, Giant barocaloric effects over a wide temperature range in superionic conductor AgI, Nat. Commun. **8**, 1851 (2017).

[6] A. K. Sagotra, D. Chu, and C. Cazorla, Room-temperature mechanocaloric effects in lithium-based superionic materials, Nat. Commun. **9**, 3337 (2018).

[7] J. F. Scott, Electrocaloric materials, Annu. Rev. Mater. Res. **41**, 229 (2011).

[8] S. Kar-Narayan and N. D. Mathur, Direct and indirect electrocaloric measurements using multilayer capacitors, J. Phys. D: Appl. Phys. **43**, 032002 (2010).

[9] E. Defay, S. Crossley, S. Kar-Narayan, X. Moya, and N. D. Mathur, The electrocaloric efficiency of ceramic and polymer films, Adv. Mater. **25**, 3337 (2013).

[10] Z. Jiang, S. Prokhorenko, S. Prosandeev, Y. Nahas, D. Wang, J. Íñiguez, E. Defay, and L. Bellaiche, Electrocaloric effects in the lead-free Ba(Zr,Ti)O_3 relaxor ferroelectric from atomistic simulations, Phys. Rev. B **96**, 014114 (2017).

[11] W. Geng, Y. Liu, X. Meng, L. Bellaiche, J. F. Scott, B. Dkhil, and A. Jiang, Giant negative electrocaloric effect in antiferroelectric La-doped Pb(Zr,Ti)O_3 thin films near room temperature, Adv. Mater. **27**, 3165 (2015).

[12] J. Mangeri, K. C. Pitike, S. P. Alpay, and S. Nakhmanson, Amplitudon and phason modes of electrocaloric energy interconversion, npj Comput. Mater. **2**, 16020 (2016).

[13] J. Zhang, S. P. Alpay, and J. A. Rossetti, Influence of thermal stresses on the electrocaloric properties of ferroelectric films, Appl. Phys. Lett. **98**, 132907 (2011).

[14] T. Tong, J. Karthik, R. V. K. Mangalam, L. W. Martin, and D. G. Cahill, Reduction of the electrocaloric entropy change of ferroelectric $PbZr_{1-x}Ti_xO_3$ epitaxial layers due to an elastocaloric effect, Phys. Rev. B **90**, 094116 (2014).

[15] S. Pandya, J. D. Wilbur, B. Bhatia, A. R. Damodaran, C. Monachon, A. Dasgupta, W. P. King, C. Dames, and L. W. Martin, Direct Measurement of Pyroelectric and Electrocaloric Effects in Thin Films, Phys. Rev. Appl. **7**, 034025 (2017).

[16] E. Defay, R. Faye, G. Despesse, H. Strozyk, D. Sette, S. Crossley, X. Moya, and N. D. Mathur, Enhanced electrocaloric efficiency via energy recovery, Nat. Commun. **9**, 1827 (2018).

[17] A. S. Mischenko, Q. Zhang, J. F. Scott, R. W. Whatmore, and N. D. Mathur, Giant electrocaloric effect in thin-film $PbZr_{0.95}Ti_{0.05}O_3$, Science **311**, 1270 (2006).

[18] B. Neese, B. Chu., S.-G. Lu, Y. Wang, E. Furman, and Q. M. Zhang, Large electrocaloric effect in ferroelectric polymers near room temperature, Science **321**, 821 (2008).

[19] B. Asbani, Y. Gagou, J.-L. Dellis, M. Trcek, Z. Kutnjak, M. Amjoud, A. Lahmar, D. Mezzane, and M. El Marssi, Lead free $Ba_{0.8}Ca_{0.2}Te_xTi_{1-x}O_3$ ferroelectric ceramics exhibiting high electrocaloric properties, J. Appl. Phys. **121**, 064103 (2017).

[20] C. Cazorla, O. Diéguez, and J. Íñiguez, Multiple structural transitions driven by spin-phonon couplings in a perovskite oxide, Sci. Adv. **3**, e1700288 (2017).

[21] C. Cazorla and J. Íñiguez, Insights into the phase diagram of bismuth ferrite from quasiharmonic free-energy calculations, Phys. Rev. B **88**, 214430 (2013).

[22] J. P. Perdew, K. Burke, and M. Ernzerhof, Generalized Gradient Approximation Made Simple, Phys. Rev. Lett. **77**, 3865 (1996).

[23] G. Kresse and J. Fürthmuller, Efficient iterative schemes for *ab initio* total-energy calculations using a plane-wave basis set, Phys. Rev. B **54**, 11169 (1996); G. Kresse and D. Joubert, From ultrasoft pseudopotentials to the projector augmented-wave method, *ibid.* **59**, 1758 (1999).

[24] P. E. Blöchl, Projector augmented-wave method, Phys. Rev. B **50**, 17953 (1994).

[25] C. Cazorla and M. Stengel, Electrostatic engineering of strained ferroelectric perovskites from first-principles, Phys. Rev. B **92**, 214108 (2015).

[26] C. Cazorla, Lattice Effects on the Formation of Oxygen Vacancies in Perovskite Thin Films, Phys. Rev. Appl. **7**, 044025 (2017).

[27] G. Kresse, J. Furthmüller, and J. Hafner, *Ab initio* force constant approach to phonon dispersion relations of diamond and graphite, Europhys. Lett. **32**, 729 (1995).

[28] D. Alfè, PHON: A program to calculate phonons using the small displacement method, Comput. Phys. Commun. **180**, 2622 (2009).

[29] C. Cazorla and J. Boronat, Simulation and understanding of atomic and molecular quantum crystals, Rev. Mod. Phys. **89**, 035003 (2017).

[30] J. Strečka and M. Jaščur, A brief account of the Ising and Ising-like models: Mean-field, effective-field and exact results, Acta Phys. Slovaca **65**, 235 (2015).

[31] X. Moya, S. Kar-Narayan, and N. D. Mathur, Caloric materials near ferroic phase transitions, Nat. Mater. **13**, 439 (2014).

[32] L. Mañosa and A. Planes, Materials with giant mechanocaloric effects: Cooling by strength, Adv. Mater. **29**, 1603607 (2017).

[33] A. A. Belik, S. Iikubo, K. Kodama, N. Igawa, S. Shamoto, S. Niitaka, M. Azuma, Y. Shimakawa, M. Takano, F. Izumi, and E. Takayama-Muromachi, Neutron powder diffraction study on the crystal and magnetic structures of $BiCoO_3$, Chem. Mater. **18**, 798 (2006).

[34] K. Oka, M. Azuma, W.-T. Chen, H. Yusa, A. A. Belik, E. Takayama-Muromachi, M. Mizumaki, N. Ishimatsu, N. Hiraoka, M. Tsujimoto, M. G. Tucker, J. P. Attfield, and Y. Shimakawa, Pressure-induced spin-state transition in $BiCoO_3$, J. Am. Chem. Soc. **132**, 9438 (2010).

[35] R. D. King-Smith and D. Vanderbilt, Theory of polarization of crystalline solids, Phys. Rev. B **47**, 1651(R) (1993).

[36] I. Ponomareva and S. Lisenkov, Bridging the Macroscopic and Atomistic Descriptions of the Electrocaloric Effect, Phys. Rev. Lett. **108**, 167604 (2012).

[37] M. Marathe, D. Renggli, M. Sanlialp, M. O. Karabasov, V. V. Shvartsman, D. C. Lupascu, A. Grünebohm, and C. Ederer, Electrocaloric effect in $BaTiO_3$ at all three ferroelectric transitions: Anisotropy and inverse caloric effects, Phys. Rev. B **96**, 014102 (2017).

[38] P. Chen, M. N. Grisolia, H. J. Zhao, O. E. González-Vázquez, L. Bellaiche, M. Bibes, B.-G. Liu, and J. Íñiguez, Energetics of oxygen-octahedra rotations in perovskite oxides from first principles, Phys. Rev. B **97**, 024113 (2018).

[39] M. Azuma, S. Niitaka, N. Hayashi, K. Oka, M. Takano, H. Funakubo, and Y. Shimakawa, Rhombohedral-tetragonal phase

boundary with high Curie temperature in $(1-x)\mathrm{BiCoO_3}$-$x\mathrm{BiFeO_3}$ solid solution, Jpn. J. Appl. Phys. **47**, 7579 (2008).

[40] H. Hojo, K. Oka, K. Shimizu, H. Yamamoto, R. Kawabe, and M. Azuma, Development of bismuth ferrite as a piezoelectric and multiferroic material by cobalt substitution, Adv. Mater. **30**, 1705665 (2018).

[41] J. Liu, M. V. Fernández-Serra, and P. B. Allen, First-principles study of pyroelectricity in GaN and ZnO, Phys. Rev. B **93**, 081205(R) (2016).

[42] J. Liu and S. T. Pantelides, Mechanisms of Pyroelectricity in Three- and Two-Dimensional Materials, Phys. Rev. Lett. **120**, 207602 (2018).